The Mechanism of Activation of Monomeric B-Raf V600E

Ryan C. Maloney[a], Mingzhen Zhang[a], Hyunbum Jang[a] and Ruth Nussinov[a,b,*]

[a] Computational Structural Biology Section, Frederick National Laboratory for Cancer Research in the Laboratory of Cancer Immunometabolism, National Cancer Institute, Frederick, MD 21702, U.S.A
[b] Department of Human Molecular Genetics and Biochemistry, Sackler School of Medicine, Tel Aviv University, Tel Aviv 69978, Israel

* Author for correspondence:
Tel: 1-301-846-5579
E-mail: NussinoR@mail.nih.gov

Declarations of interest: none

Abstract

Oncogenic mutations in the serine/threonine kinase B-Raf, particularly the V600E mutation, are frequent in cancer, making it a major drug target. Although much is known about B-Raf's active and inactive states, questions remain about the mechanism by which the protein changes between these two states. Here, we utilize molecular dynamics to investigate both wild-type and V600E B-Raf to gain mechanistic insights into the impact of the Val to Glu mutation. The results show that the wild-type and mutant follow similar activation pathways involving an extension of the activation loop and an inward motion of the αC-helix. The V600E mutation, however, destabilizes the inactive state by disrupting hydrophobic interactions present in the wild-type structure while the active state is stabilized through the formation of a salt bridge between Glu600 and Lys507. Additionally, when the activation loop is extended, the αC-helix is able to move between an inward and outward orientation as long as the DFG motif adopts a specific orientation. In that orientation Phe595 rotates away from the αC-helix, allowing the formation of a salt bridge between Lys483 and Glu501. These mechanistic insights have implications for the development of new Raf inhibitors.
Keywords: B-Raf, oncogene, kinase, protein structure, activation mechanism

1. Introduction

The Ras/Raf/MEK/ERK signaling pathway, also called the mitogen activated protein kinase (MAPK) pathway, is an important route for controlling cell life cycle events.[1-3] Dysregulation of the MAPK pathway negatively has been linked to several diseases including cancer and RASopathies such as LEOPARD and Noonan syndromes.[4,5] The Raf family of serine/threonine protein kinases, which is composed of A-Raf, B-Raf, and C-Raf (also called Raf-1), is a key component of the MAPK pathway.[6] The members of the Raf family share three conserved regions (CRs) (Figure 1a).[7] CR1 is involved in autoinhibition and membrane recruitment and contains two subdomains: the Ras binding domain (RBD) and the cysteine-rich domain (CRD). CR2 is a flexible linker between CR1 and CR3 and contains a serine/threonine rich region that can be phosphorylated and binds to 14-3-3 scaffolding proteins. CR3 is the kinase domain (Figure 1b) that, upon activation, can phosphorylate its substrate proteins MEK1 and MEK2. The kinase domain consists of two lobes connected by a short hinge region (Figure 1c).[8] The N-terminal lobe, the smaller of the two, contains five β-sheets and an α-helix called the C helix (αC-helix). Between β1 and β2 is the phosphate loop (P-loop, residues 462-469) which stabilizes ATP phosphate groups. The C-terminal lobe contains six α-helices as well as the activation loop (A-loop, residues 593-622) which begins with the conserved DFG motif (residues 594-596). Between these two lobes is the ATP binding pocket.

Among the three members of the Raf family, B-Raf is subject to a particularly large number of oncogenic mutations. B-Raf mutations are found in more than 50% of melanomas, as well as being prevalent in thyroid, ovarian, and colorectal cancers.[9] These mutations are grouped into three classes.[10] Mutations involving B-Raf V600 residue belong to Class I. B-Raf with a Class I mutation is constitutively active as a monomer, independent of activation by Ras and dimerization.[11] Class II mutations are also kinase activated mutations; however, these mutations occur on residues in AS-H1 (residues 597-604), P-loop including Gly464 and Gly469, and activation segment involving Leu597 and Lys601.[10] These mutations are active independent from Ras, like class I mutations, but they require B-Raf homodimerization. The final class of B-Raf mutations, class III mutations, also occur on residues other than V600; however, they are kinase impaired mutations. These Class III mutations require activation via Ras mutants and heterodimerization with C-Raf wild type.[12,13]

Nearly 90% of all B-Raf mutations are the Class I V600E mutation, and as such it is important to understand the activation mechanism of this mutation.[14,15] In the inactive state, monomeric wild type B-Raf adopts an autoinhibited conformation in the cytosol. B-Raf is recruited to the membrane through a combination of interactions between the RBD with active Ras [16-18] and the CRD with the cell membrane.[19,20] This releases B-Raf from the autoinhibited state and effectively increases the concentration of B-Raf near the cell membrane.[21] Upon recruitment to the membrane, B-Raf is activated through kinase domain dimerization, and two residues Thr599 and Ser602 in the A-loop are phosphorylated.[22-24] The phosphorylated residues destabilize the inactive state and stabilizes the active state. Once B-Raf adopts the active configuration, the substrate MEK1/2 protein can bind to the catalytic cleft of B-Raf and be phosphorylated.[25,26]

Switching from the inactive to the active conformation, B-Raf exhibits several characteristic structural changes.[7] In the inactive conformation, the αC-helix adopts an outward position and a collapsed A- loop with an inhibitory helix called AS-H1 (Figure 1d).[27] The DFG motif can also adopt an outward position in which the Phe595 side chain flips outward to occupy the position normally occupied by the Asp594 side chain, preventing ATP from entering the

binding pocket.[28] In the active configuration, the αC-helix and DFG adopt an inward position and the A-loop extends, eliminating the inhibitory AS-H1 helix.[29] The inward position of the αC-helix causes the formation of a salt bridge between Glu501 of the αC-helix and Lys483 in the β3 strand.[4,30,31] The inward position of the DFG motif allows Asp594 to interact with Mg^{2+} bound to ATP. Unlike wild type B-Raf, which requires membrane recruitment and dimerization for activation, B-Raf V600E is constitutively active as a monomer. [9,32] It has been proposed that the substitution of Val600 with the negatively charged Glu acts as a mimic of the two phosphorylated A-loop residues, however the available crystal structures lacking the phosphorylated A-loop residues have been unable to confirm this. It has also been suggested that a salt-bridge between Glu600 and Lys507 on the αC-helix in B-Raf V600E mutant is crucial for the formation of the active conformation.[33] Further knowledge detailing the structural differences between monomeric wild type and V600E B-Raf could reveal novel targets for the development of inhibitors.

We perform molecular dynamics (MD) simulations on B-Raf wild type and V600E mutant monomers. Unlike in previous work which simulated either B-Raf bound to inhibitors or with an empty ATP binding pocket, we have included ATP in our structures. Results show that even with the V600E mutation, the AS-H1 helix is still present, however these residues do show greater fluctuation than in the wild type simulations, indicating that the mutation has destabilized this inhibitory helix. In addition, simulations show that when the A-loop is extended, the αC-helix can move between the inward and outward positions if the DFG motif remains in an active configuration. These results aid in our understanding of the activation mechanism of B-Raf V600E. We provide detailed analysis linking the motion of the αC-helix to the orientation of the DFG motif. Importantly, these results indicate that the B-Raf V600E mutation results in an activation mechanism that mimics the mechanism of wild-type B-Raf.

2. Materials and Methods

Initial coordinates for the B-Raf kinase domain (residues 449 to 720) were adopted from the crystal structures (PDB IDs: 3OG7 [V600E active conformation], 4MNE [WT active conformation in complex with MEK], 4MNF [V600E active conformation], 4XV2 [V600E inactive conformation], 5ITA [WT intermediate conformation], 6U2G [WT inactive conformation in complex with MEK], 6U2H [WT active conformation in complex with 14-3-3]). Monomeric B-Raf structures were modeled by selecting the best resolved protomer in the crystal structures of Raf dimers, and any other proteins in the crystal structures were removed. Inhibitors present in the crystal structure were replaced with ATP and Mg^{2+}. The initial configurations are shown in Figure S1 and structural details of these configurations are summarized in Table 1. We focused on initial conditions with the DFG-in configuration, as the DFG-out configuration would cause the Phe595 to overlap with the ATP phosphates. From there, we selected Raf structures in which the αC-helix exhibited either an inward, outward, or intermediate orientation. Missing residues in the ATP binding P-loop and A-loop were modeled using the CHARMM program,[34] and any mutated residues present, except for residue 600, were changed back to the wild-type sequence. Residue 600 was either kept as Val to obtain the B-Raf wild type or mutated to Glu obtain B-Raf V600E. The A-loop was modeled to have either an "extended" or "collapsed" configuration. Structures with a collapsed A-loop, with the exception of configuration *h*, exhibit the AS-H1 inhibitory helix in the initial A-loop structure. For configuration h the inhibitory helix is not present, but A-loop residues are positioned near the main body of the protein.

The B-Raf monomers with ATP and Mg^{2+} were placed in a periodic box of $\sim 100 \times 100 \times 100\ \text{Å}^3$ and the explicit TIP3 water model was used to solvate the system. Water molecules within 2.6 Å of B-Raf were removed to prevent atom collapse. Sodium (Na^+) and chlorine (Cl^-) ions were added to generate a final ionic strength of ~ 100 mM and neutralize the system. During the preequilibration stage, a series of minimization cycles were performed for the solvents including ions with the harmonically restrained protein backbone until the solvent reached 310 K. Following the energy minimization steps, a series of dynamic cycles were performed by gradually releasing the harmonic constraints on the protein backbone with the long-range electrostatics calculation using the particle mesh Ewald (PME) method. The production runs of all-atom MD simulations were conducted using the NAMD package (version 2.12)[35] with the updated CHARMM[34] all-atom force field (version 36m).[36,37] All simulations closely followed the same protocol as in our previous studies.[38-55] In the productions runs, the Langevin thermostat maintained the constant temperature at 310 K and the Nosé-Hoover Langevin piston pressure control sustained the pressure at 1.01325 bar (1 atm) with the NPT condition. A 2 fs timestep was used for 5×10^8 steps for all simulations. A total of 13 μs simulation were performed for 13 systems, each with 1 μs simulation time. Trajectory information was collected every 5×10^4 steps (100 ps).

3 Results

3.1 Wild-Type B-Raf Kinase Domain

First, we look at the features present in the active and inactive conformations of wild-type B-Raf. To get a broad picture of the movement of B-Raf, Figure 2a shows the root mean square fluctuation (RMSF) for wild-type B-Raf simulations that begin with an inward (configurations *j* in Table 1), intermediate (*l*), or outward αC-helix (*m*). (Results for all simulations provided in Figure S2). In general, the simulations show a flexible region at the P-loop, the N-terminal end of the αC-helix, the residues of β4 through β5, the A-loop, and the residues around the αG-helix. These regions are highlighted in red in the snapshots in Figure 2b, which are colored according to b-factor values. The A-loop and P-loop are known to be highly flexible, indeed many of the crystal structures in the protein data bank lack density information for these residues. The fluctuations of the N-terminal end of the αC-helix are also expected because these are the residues that move most when the αC-helix changes between inward and outward orientations. The β4 and β5 strands are in the N-lobe just before the hinge region that connects the N-lobe and C-lobe. The αG-helix is important in B-Raf/MEK binding[56], and previous simulations of B-Raf with an empty ligand binding pocket have found a possible transition state for the active-inactive transition in which this helix is partially unfolded.[33] The RMSF values for these three configurations closely match each other for most residues, however both simulations that began with an inward αC-helix did have local peaks of large RMSF values. The N-terminal end of the αC-helix is most flexible for configuration *j*, and the A-loop is most flexible for configuration *l*. These regions are investigated in more detail below to identify the differences in the active and inactive wild-type B-Raf structures.

A widely reported hallmark of active kinases is an "inward" position of the αC-helix. This inward position allows for the formation of a salt bridge between Lys483 of the β3 strand and Glu501 of the αC-helix of B-Raf. We plot the distance between the β carbon (CB) atoms on Lys483 and Glu501 in Figure 3a for the wild-type simulations. The results from all simulations are in Figure S3. This distance indicates if the Lys483-Glu501 salt bridge is present, which gives an indication of the αC-helix position throughout the simulations. The simulations that began

with an inward αC-helix exhibited a mostly stable salt-bridge that had a distance of $\sim 8.2 - 8.75$ Å between the CB atoms. There is, however, a region of ~ 700 ns during which the salt bridge of configuration *j* repeatedly broke and reformed. We can see from the snapshots in Figure 3b that when the salt bridge is broken the αC-helix moves outward and when the salt bridge is present, the αC-helix moves inward. This inward and outward motion of the αC-helix could account for the large RMSF values of configuration *j* in this region. The simulation that began with the intermediate αC-helix and collapsed A-loop (configuration *l*) had a salt bridge distance of ~ 10 Å at the beginning of the simulation. The Lys483 and Glu501 residues move closer together for the first ~ 300 ns, after which these residues move gradually apart for the remainder of the simulation, to a distance of ~ 13 Å. The simulation that began with an outward αC-helix (configuration *m*) maintained this orientation throughout the course of the simulation, with the distance between Lys483 and Glu501 of ~ 15 Å. The position of the αC-helix can also be measured by calculating the distance between the centers of mass of the αC-helix and the C-lobe.[57] The results of these calculations are shown in Figure S4a. Also presented in Figure S4b is the distance between the amide nitrogen (NZ) in the sidechain of Lys483 and the carboxylate carbon (CD) in the sidechain of Glu501. These data follow the same trends as shown in Figure 3a and show that the formation of the salt bridge between Lys483 and Glu501 is tied to the inward motion of the αC-helix.

A second important feature that distinguishes active and inactive B-Raf is an extended activation loop for the active kinase. Although it is not expected to be the most stable configuration, monomeric wild-type B-Raf simulations that started with an extended A-loop maintained it throughout the simulation. Configuration *j* shows that the extended A-loop may be stabilized through hydrophobic interactions between Val600, Val504, Ile572, and Ala598 along with hydrogen bonds between β6 and β9 (Figure 4a).[58] Configuration *m* shows that the collapsed A-loop with inhibitory AS-H1 helix is stabilized through formation of a hydrophobic pocket that includes Val600 along with residues Leu485, Val487, Phe498, Val502, Phe516, Ile527, and Leu597 (Figure 4b). These stabilizing interactions may explain why both configurations *j* and *m* showed low RMSF values in the A-loop up to residue 600. Configuration *l* shows that the extended A-loop with the inhibitory AS-H1 helix does not form these stabilizing interactions: Val600 is not in a hydrophobic pocket and β9 is not positioned to create hydrogen bonds with β6 (Figure 4c). This could explain why the RMSF values for the A-loop of configuration *l* is larger than those of configurations *j* and *m*.

3.2 Active B-Raf V600E

The B-Raf V600E simulations that began with an inward αC-helix behaved much the same as the an inward αC-helix wild-type B-Raf. Superimposed snapshots in Figure 5a of the active wild-type (configuration *f*) and mutant B-Raf (configurations *a-d*) show that they largely share the same structural features. In these snapshots, the residues of the A-loop after Ser605 and the residues around the αG-helix (Gln653 to Val681) show the largest differences in position between the wild-type and mutant configurations. These residues also display the greatest values in the RMSF as shown in Figure 5b. RMSF results also show that active B-Raf V600E generally displays larger RMSF values in the activation loop than the active wild-type B-Raf (see Figure S2). The Lys483-Glu501 salt bridge is stable through the course of the simulations for configurations *a-d*, however in configuration *e* the salt bridge broke and reformed throughout the final 700 ns of the simulation (see Figure 6c and Figure S3). This is similar to the breaking and reforming of the salt bridge that was seen in wild-type B-Raf configuration *j* (Figure 3a). Unlike

configuration *j*, the B-Raf V600E configuration *e* showed an outward shift in the αC-helix along with the breaking of the salt bridge, as can be seen in Figure S5.

In the active wild-type B-Raf, Val600 formed hydrophobic interactions with two nearby residues while the A-loop was extended. In B-Raf V600E, it has been proposed the Glu600 forms a salt bridge with Lys507. Enhanced-sampling simulations have found that this salt bridge is not stable and have instead proposed a possible salt bridge between Glu600 and Arg603.[33] We plot the distances between the Glu600 carboxylate carbon (CD) and the Lys507/Arg603 amide nitrogen (NZ) in Figure 6a and 6b, respectively. This shows that the Lys507-Glu600 salt bridge remains relatively stable through most of the simulation, but it does break and quickly reform periodically. The salt-bridge between Arg603 and Glu600 is much less stable, though may play a secondary role in stabilizing the extended A-loop.

3.3 Inactive B-Raf V600E

The simulations that begin with intermediate or outward oriented αC-helix display distinct behavior from their wild-type counterparts. Although none of these simulations moved from the inactive to the active state, as other simulations have reported,[57] there are indications how this mutation may destabilize the inactive configuration. As was the case in the active structures, the RMSF values of the A-loop residues are greater for the inactive B-Raf V600E structures than for wild-type inactive structures (Figure 7a, b). This could indicate that the mutation from Val to Glu destabilizes the hydrophobic pocket occupied by Val600 in wild-type B-Raf. There is also a distinct difference in the αC-helix behavior of the V600E mutant simulations (configurations *f* and *g*) with an intermediate αC-helix in the initial configuration compared to the wild-type. In these V600E mutant systems, the Lys483 and Glu501 residues remain ∼10 Å apart and did not move away from each other, as was seen in the wild type system (configuration *l*) (Figure 7c, d). The configurations that began with an outward αC-helix maintained this orientation throughout the simulation.

The inactive mutant systems also display different Glu600 salt bridge formation than was seen in active B-Raf V600E. Configuration *f*, which had an extended A-loop in the initial configuration, did show the formation of salt bridge between Lys507 and Glu600 (Figure 8a). The other inactive mutant systems, configurations *g*, *h*, and *i*, had collapsed A-loops and did not form this salt bridge. Instead, these inactive B-Raf V600E systems showed that the salt bridge between Glu600 and Arg603 (Figure 8b), was much more prevalent than was seen in the active B-Raf V600E systems (Figure 6b). The formation of this salt bridge could stabilize the collapsed A-loop with the inhibitory AS-H1 helix, even though the V600E mutation would disrupt the hydrophobic pocket occupied by V600, shown in Figure 4b.

Link between activation loop and αC-helix position

To understand the differences in the activation loop behavior of B-Raf, we look at the DFG motif (residues 594-596), which is located at the beginning of the A-loop. Inhibitors are known to bind to B-Raf with the Phe residue of the DFG motif in either an in or out orientation. In the out orientation, the phenylalanine ring occupies the ATP binding pocket and is thus incompatible with our monomeric B-Raf with ATP simulations. Indeed, when we measure the position of this residue, we find that it maintains an inward orientation throughout the course of the simulation. Of more interest is the orientation of the dihedral angles around the XDFG motif (DFG motif plus the preceding Gly593 in B-Raf). It has been proposed that kinases can be classified as active or inactive based on the backbone dihedrals □ and ψ of the residues, Gly593, Asp594, and Phe595, along with the first side chain dihedral, χ_1, of Phe595.[59] Specifically, they found that all catalytically primed structures exhibit a "BLAminus" conformation, that is the

backbone dihedrals of the X residue (Gly593) occupies the β (B) region of Ramachandran map, Asp594 occupies the left (L) region, and Phe595 occupies the α (A) region. Finally, the side chain of Phe595 adopts a χ_1 gauche-minus (-60°) rotamer. The BLAminus conformation is the only one that properly positioned the DFG motif and A-loop to simultaneously bind ATP, magnesium ion, and substrate. Figure S6 shows how the XDFG dihedral angles evolved over the course of each simulation.

Simulations that began with an inward αC-helix and extended A-loop all displayed the BLA-minus XDFG dihedral orientation throughout the course of the simulation (Figure S6, configurations *a-e* for B-Raf V600E and *j-k* for wild-type B-Raf). An example of this can be seen for configuration *j* in Figure 9a. In this simulation, B-Raf V600E maintains the BLA configuration for the backbone dihedrals, even during the time period when the αC-helix switches repeatedly between the inward and outward orientation (Figure 3a). The Phe595 χ_1 dihedral oscillates between -90° and -50° throughout the simulation (Figure 9b). This fluctuation can be expected from the nature of molecular dynamics simulation, but importantly the χ_1 angle never switches to trans (180°) or gauche-plus (60°). A snapshot of the DFG region for this configuration is shown Figure 9c. Therefore, we can conclude that this configuration adopts the BLAminus orientation and is an active kinase. The inward αC-helix B-Raf simulations (configurations *a-e*, *k*) also exhibit the BLAminus XDFG orientation, even configuration *e* when the salt bridge was breaking and reforming (Figures S3 and S4).

One of the B-Raf V600E simulations with an intermediate αC-helix, configuration *f*, had an initial XDFG orientation of BLAminus but changed to BLAtrans in the final ~300 ns of the simulation (Figure 10a, b). The change in the Phe595 χ_1 gauche rotamer from minus to trans moves the phenylalanine side chain into the pocket between the αC-helix and β3 (Figure 10c). Figure 7c showed that this configuration did have an inward orientation of the αC-helix through much of the first ~700 ns of the simulation, but not for the final 300 ns. This can be seen even more clearly by plotting the distance between the amide nitrogen (NZ) in the sidechain of Lys483 and the carboxylate carbon (CD) in the sidechain of Glu501 (Figure 10d). This shows that after the Phe595 χ_1 gauche rotamer becomes trans, the Lys483-Glu501 salt-bridge can no longer form and highlights the importance of the positioning of this residue on kinase activation.[60]

For the remaining inactive B-Raf structures (configurations *g-i* for B-Raf V600E and *l-m* for wild-type B-Raf) we see two general trends. First, none of these inactive structures ever displayed the active BLAminus XDFG orientation. Second, the inactive wild-type B-Raf configurations and inactive B-Raf V600E configurations displayed different behavior around the DFG motif, even when starting from the same initial configuration. Configuration *g* (B-Raf V600E, intermediate αC-helix) started with a BLAplus orientation and changed to a BLAtrans orientation. The BLAtrans orientation matches the final orientation of configuration *f*, which was based on the same crystal structure as configuration *g*. Configuration *l* (wild-type B-Raf, intermediate αC-helix based on the same crystal structure as configurations *f* and *g*) also began with a BLAplus orientation (like configuration *g*), but ended with an ABAminus orientation. This marks a larger change away from the active configuration for the wild-type structure than the V600E structure. In a similar manner, the B-Raf V600E mutant with an outward αC-helix (configuration *i*) changed from BLBplus to BLBtrans and then again to BLBminus, while the wild type (configuration *m*) maintained the BLBplus throughout the simulation. Taken together, we see that in the inactive configurations, the mutant and wild type structures based on the same initial PDBs do not exhibit the same dynamics around the DFG motif through the course of the

simulations. This can also be seen in the cross correlation data in Figure S7: while the configurations with an inward orientation of the αC-helix all display similar results, in configurations with intermediate or outward αC-helix the results from the V600E mutant and wild type simulations do not match each other, even when starting from the same PDB structures.

Another way to visualize the link between the αC-helix and the activation loop is through the radius of gyration (R_g). Figure 11 shows the probability distribution of the radius of gyration versus the distance between Lys483 and Glu501. The general trend is that systems with an outward orientation of the αC-helix (large distance between Lys483 and Glu501) display a compact A-loop with low value of R_g. Systems with an inward αC-helix with small distance between Lys483 and Glu501, conversely, have an extended A-loop with large values of R_g. More specifically, these results show that the B-Raf V600E simulations sample more of the phase space as shown by the broader regions of high probability. In addition, while the wild-type B-Raf that began with an intermediate αC-helix relaxes to a state similar to the outward αC-helix simulations, the B-Raf V600E simulations with an intermediate αC-helix appear to occupy an intermediate state. This trend coupled with the XDFG dihedral results shows that the activation loop position has a large impact on the αC-helix.

4 Discussion and Conclusion

B-Raf has been widely studied over the past decades.[61-63] Yet despite this, key features of B-Raf activation remain elusive. It is known that inactive B-Raf can exhibit, among other features, an outward placement of the αC-helix, an inhibitory loop called AS-H1 in the activation loop, and a disassembled regulatory spine.[64] In going from an inactive to the active confirmation, B-Raf dimerizes with another Raf protein, has an inward placement of the αC-helix, an extended activation loop, and stacks four hydrophobic residues into a regulatory spine.[65] Understanding of how B-Raf moves between the active and inactive states could aid in targeted drug development. This is particularly important for the B-Raf V600E mutation, a so-called class I mutation that is a constitutively active monomer independent of its upstream activator, Ras.

This work builds upon previous simulation studies of monomeric B-Raf to further our understanding of the mechanism of activation for B-Raf V600E. Previous MD simulations of monomeric B-Raf with an empty ATP binding pocket have found that wild type B-Raf with an initially active configuration will quickly convert to an inactive conformation through the formation of the AS-H1 helix and an outward movement of the αC-helix.[57] We do not observe this in our simulations which include ATP and the magnesium ion, a requirement for a kinase action. Instead, active wild type B-Raf remains primarily in the active configuration. The αC-helix predominately remains inward, as noted by the persistence of the Lys483-Glu501 salt bridge. The reason for these differences could be due to the interaction between the DFG-Asp residue and the magnesium ion in the ATP pocket. This interaction could stabilize the residues around the DFG motif, preventing the formation of the inhibitory helix. It has also been reported that active V600E will maintain an active conformation with an inward αC-helix [57]. While most of our simulations agree with this, there were results that indicate that the αC-helix of active B-Raf V600E can switch between the inward and outward conformations yet maintain an active BLAminus XDFG orientation. It is only when the DFG-Phe χ_1 dihedral switched from minus to trans did the αC-helix become fixed in the outward position. This suggests that adopting the BLAminus XDFG orientation is a prerequisite for inward motion of the αC-helix. This insight

could aid in the development of inhibitors that prevent the DFG motif from adopting this orientation.

Both B-Raf wild type and V600E simulations which started with the AS-H1 helix maintained this inhibitory loop throughout the course of the simulation. Others have posited that the V600E mutation should disrupt this inhibitory loop due to the mutation of the hydrophobic Val with the negatively charged Glu. Although our simulations do not show the unwrapping of the inhibitory loop, the higher RMSF in the activation loop of the V600E simulations indicate that Glu mutation does increase the flexibility of this loop compared to Val. The persistence of the AS-H1 loop, even with the Glu mutation, indicates that breaking this short helix could be the highest energy barrier in moving from the inactive to active configuration.

To conclude, we have performed extensive MD simulations on wild-type and V600E B-Raf. For the first time these simulations include the physiologically important ATP molecule. Our results indicate that the V600E mutation results in activation via a mechanism that mirrors that seen in wild-type B-Raf. This has also been the case in PI3Kα and PTEN, and we expect is a general phenomenon.[66] We found that the αC-helix was only switched between the inward and outward orientation when the DFG motif adopted a BLAminus orientation and suggest that this information could assist in designing B-Raf inhibitors that exploit this feature.

5 Author contributions

Ryan Maloney: Investigation, Formal Analysis, Writing – Original Draft. **Mingzhen Zhang**: Writing – Review & Editing. **Hyunbum Jang**: Conceptualization, Methodology, Writing – Review & Editing. **Ruth Nussinov**: Conceptualization, Supervision, Project administration, Funding acquisition, Writing – Review & Editing.

6 Acknowledgements

This project has been funded in whole or in part with federal funds from the National Cancer Institute, National Institutes of Health, under contract HHSN26120080001E. The content of this publication does not necessarily reflect the views or policies of the Department of Health and Human Services, nor does mention of trade names, commercial products or organizations imply endorsement by the US Government. This research was supported [in part] by the Intramural Research Program of the NIH, National Cancer Institute, Center for Cancer Research. The calculations had been performed using the high-performance computational facilities of the Biowulf PC/Linux cluster at the National Institutes of Health, Bethesda, MD (https://hpc.nih.gov/).

References

1 Pfister, S. *et al.* BRAF gene duplication constitutes a mechanism of MAPK pathway activation in low-grade astrocytomas. *Journal of Clinical Investigation* **118**, 1739-1749, doi:10.1172/jci33656 (2008).

2 Lavoie, H. & Therrien, M. Regulation of RAF protein kinases in ERK signalling. *Nature Reviews Molecular Cell Biology* **16**, 281-298, doi:10.1038/nrm3979 (2015).

3 Tsai, C. J. & Nussinov, R. Allosteric activation of RAF in the MAPK signaling pathway. *Current Opinion in Structural Biology* **53**, 100-106, doi:10.1016/j.sbi.2018.07.007 (2018).

4 Kornev, A. P., Haste, N. M., Taylor, S. S. & Ten Eyck, L. F. Surface comparison of active and inactive protein kinases identifies a conserved activation mechanism.

Proceedings of the National Academy of Sciences of the United States of America **103**, 17783-17788, doi:10.1073/pnas.0607656103 (2006).

5 Razzaque, M. A. *et al.* Germline gain-of-function mutations in RAF1 cause Noonan syndrome. **39**, 1013-1017 (2007).

6 Tran, N. H., Wu, X. C. & Frost, J. A. B-Raf and Raf-1 are regulated by distinct autoregulatory mechanisms. *Journal of Biological Chemistry* **280**, 16244-16253, doi:10.1074/jbc.M501185200 (2005).

7 Shaw, A. S., Kornev, A. P., Hu, J. C., Ahuja, L. G. & Taylor, S. S. Kinases and Pseudokinases: Lessons from RAF. *Molecular and Cellular Biology* **34**, 1538-1546, doi:10.1128/mcb.00057-14 (2014).

8 Taylor, S. S., Keshwani, M. M., Steichen, J. M. & Kornev, A. P. Evolution of the eukaryotic protein kinases as dynamic molecular switches. *Philosophical Transactions of the Royal Society B-Biological Sciences* **367**, 2517-2528, doi:10.1098/rstb.2012.0054 (2012).

9 Davies, H. *et al.* Mutations of the BRAF gene in human cancer. *Nature* **417**, 949-954, doi:10.1038/nature00766 (2002).

10 Śmiech, M., Leszczyński, P., Kono, H., Wardell, C. & Taniguchi, H. Emerging BRAF Mutations in Cancer Progression and Their Possible Effects on Transcriptional Networks. *Genes (Basel)* **11** (2020).

11 Yao, Z. *et al.* BRAF Mutants Evade ERK-Dependent Feedback by Different Mechanisms that Determine Their Sensitivity to Pharmacologic Inhibition. *Cancer Cell* **28**, 370-383 (2015).

12 Yao, Z. *et al.* Tumours with class 3 BRAF mutants are sensitive to the inhibition of activated RAS. *Nature* **548**, 234-238 (2017).

13 Lin, Q. *et al.* The association between BRAF mutation class and clinical features in BRAF-mutant Chinese non-small cell lung cancer patients. *J Transl Med* **17**, 298 (2019).

14 Holderfield, M., Deuker, M. M., McCormick, F. & McMahon, M. Targeting RAF kinases for cancer therapy: BRAF-mutated melanoma and beyond. *Nature Reviews Cancer* **14**, 455-467, doi:10.1038/nrc3760 (2014).

15 Durrant, D. E. & Morrison, D. K. Targeting the Raf kinases in human cancer: the Raf dimer dilemma. **118**, 3-8 (2018).

16 Lu, S. Y., Jang, H., Gu, S., Zhang, J. & Nussinov, R. Drugging Ras GTPase: a comprehensive mechanistic and signaling structural view. *Chemical Society Reviews* **45**, 4929-4952, doi:10.1039/c5cs00911a (2016).

17 Travers, T. *et al.* Molecular recognition of RAS/RAF complex at the membrane: Role of RAF cysteine-rich domain. *Scientific Reports* **8**, doi:10.1038/s41598-018-26832-4 (2018).

18 Nussinov, R., Tsai, C. J. & Jang, H. Does Ras Activate Raf and PI3K Allosterically? *Frontiers in Oncology* **9**, doi:10.3389/fonc.2019.01231 (2019).

19 Improta-Brears, T., Ghosh, S. & Bell, R. M. Mutational analysis of Raf-1 cysteine rich domain: Requirement for a cluster of basic aminoacids for interaction with phosphatidylserine. **198**, 171-178 (1999).

20 Li, S., Jang, H., Zhang, J. & Nussinov, R. Raf-1 Cysteine-Rich Domain Increases the Affinity of K-Ras/Raf at the Membrane, Promoting MAPK Signaling. **26**, 513-525.e512 (2018).

21 Nussinov, R., Tsai, C. J. & Jang, H. in *Curr Opin Struct Biol* Vol. 62 140-148 (© 2020 Elsevier Ltd, 2020).
22 Weber, C. K., Slupsky, J. R., Kalmes, H. A. & Rapp, U. R. Active Ras Induces Heterodimerization of cRaf and BRaf. *Cancer Research* **61**, 3595 (2001).
23 Hu, J. *et al.* Allosteric Activation of Functionally Asymmetric RAF Kinase Dimers. *Cell* **154**, 1036-1046 (2013).
24 Pantsar, T. The current understanding of KRAS protein structure and dynamics. **18**, 189-198 (2020).
25 Morrison, D. K., Heidecker, G., Rapp, U. R. & Copeland, T. D. Identification of the major phosphorylation sites of the Raf-1 kinase. *J Biol Chem* **268**, 17309-17316 (1993).
26 Tong, M. & Seeliger, M. A. Targeting Conformational Plasticity of Protein Kinases. *ACS Chem. Biol.* **10**, 190-200 (2015).
27 Thevakumaran, N. *et al.* Crystal structure of a BRAF kinase domain monomer explains basis for allosteric regulation. **22**, 37-43 (2015).
28 Waizenegger, I. C. *et al.* in *Mol Cancer Ther* Vol. 15 354-365 (©2016 American Association for Cancer Research., 2016).
29 King, A. J. *et al.* in *Cancer Res* Vol. 66 11100-11105 (2006).
30 Meharena, H. S. *et al.* Deciphering the structural basis of eukaryotic protein kinase regulation. *PLoS Biol* **11**, e1001680, doi:10.1371/journal.pbio.1001680 (2013).
31 Roskoski, R., Jr. Classification of small molecule protein kinase inhibitors based upon the structures of their drug-enzyme complexes. *Pharmacol Res* **103**, 26-48, doi:10.1016/j.phrs.2015.10.021 (2016).
32 Wan, P. T. *et al.* Mechanism of activation of the RAF-ERK signaling pathway by oncogenic mutations of B-RAF. *Cell* **116**, 855-867, doi:10.1016/s0092-8674(04)00215-6 (2004).
33 Marino, K. A., Sutto, L. & Gervasio, F. L. The Effect of a Widespread Cancer-Causing Mutation on the Inactive to Active Dynamics of the B-Raf Kinase. *Journal of the American Chemical Society* **137**, 5280-5283, doi:10.1021/jacs.5b01421 (2015).
34 Brooks, B. R. *et al.* CHARMM: The biomolecular simulation program. *Journal of Computational Chemistry* **30**, 1545-1614, doi:10.1002/jcc.21287 (2009).
35 Phillips, J. C. *et al.* Scalable molecular dynamics with NAMD. *J Comput Chem* **26**, 1781-1802 (2005).
36 Klauda, J. B. *et al.* Update of the CHARMM all-atom additive force field for lipids: validation on six lipid types. *J Phys Chem B* **114**, 7830-7843 (2010).
37 Huang, J. *et al.* CHARMM36m: an improved force field for folded and intrinsically disordered proteins. *Nat Methods* **14**, 71-73 (2017).
38 Chakrabarti, M., Jang, H. & Nussinov, R. Comparison of the Conformations of KRAS Isoforms, K-Ras4A and K-Ras4B, Points to Similarities and Significant Differences. *J Phys Chem B* **120**, 667-679 (2016).
39 Chavan, T. S. *et al.* High-Affinity Interaction of the K-Ras4B Hypervariable Region with the Ras Active Site. *Biophys J* **109**, 2602-2613 (2015).
40 Haspel, N., Jang, H. & Nussinov, R. in *Biophys J* (© 2020 Biophysical Society, 2020).
41 Jang, H. *et al.* Mechanisms of membrane binding of small GTPase K-Ras4B farnesylated hypervariable region. *J Biol Chem* **290**, 9465-9477 (2015).
42 Jang, H., Banerjee, A., Chavan, T., Gaponenko, V. & Nussinov, R. Flexible-body motions of calmodulin and the farnesylated hypervariable region yield a high-affinity

interaction enabling K-Ras4B membrane extraction. *J Biol Chem* **292**, 12544-12559 (2017).
43 Jang, H. *et al.* in *Structure* Vol. 27 1647-1659 e1644 (© 2019 Elsevier Ltd, 2019).
44 Li, S., Jang, H., Zhang, J. & Nussinov, R. in *Structure* Vol. 26 513-525 e512 (© 2018 Elsevier Ltd, 2018).
45 Liao, T. J., Jang, H., Fushman, D. & Nussinov, R. Allosteric KRas4B Can Modulate SOS1 Fast and Slow Ras Activation Cycles. *Biophys J* **115**, 629-641 (2018).
46 Liao, T. J., Jang, H., Fushman, D. & Nussinov, R. SOS1 interacts with Grb2 through regions that induce closed nSH3 conformations. *J Chem Phys* **153**, 045106 (2020).
47 Liao, T. J., Jang, H., Tsai, C. J., Fushman, D. & Nussinov, R. The dynamic mechanism of RASSF5 and MST kinase activation by Ras. *Phys Chem Chem Phys* **19**, 6470-6480 (2017).
48 Muratcioglu, S., Jang, H., Gursoy, A., Keskin, O. & Nussinov, R. PDEδ Binding to Ras Isoforms Provides a Route to Proper Membrane Localization. *J Phys Chem B* **121**, 5917-5927, doi:10.1021/acs.jpcb.7b03035 (2017).
49 Ozdemir, E. S. *et al.* Unraveling the molecular mechanism of interactions of the Rho GTPases Cdc42 and Rac1 with the scaffolding protein IQGAP2. *J Biol Chem* **293**, 3685-3699 (2018).
50 Ozdemir, E. S., Jang, H., Gursoy, A., Keskin, O. & Nussinov, R. Arl2-Mediated Allosteric Release of Farnesylated KRas4B from Shuttling Factor PDEδ. *J Phys Chem B* **122**, 7503-7513, doi:10.1021/acs.jpcb.8b04347 (2018).
51 Zhang, M., Jang, H., Gaponenko, V. & Nussinov, R. Phosphorylated Calmodulin Promotes PI3K Activation by Binding to the SH(2) Domains. *Biophys J* **113**, 1956-1967 (2017).
52 Zhang, M., Jang, H. & Nussinov, R. The mechanism of PI3Kα activation at the atomic level. *Chem Sci* **10**, 3671-3680 (2019).
53 Zhang, M., Jang, H. & Nussinov, R. The structural basis for Ras activation of PI3Kα lipid kinase. *Phys Chem Chem Phys* **21**, 12021-12028 (2019).
54 Zhang, M. *et al.* Ca(2+)-Dependent Switch of Calmodulin Interaction Mode with Tandem IQ Motifs in the Scaffolding Protein IQGAP1. *Biochemistry* **58**, 4903-4911, doi:10.1021/acs.biochem.9b00854 (2019).
55 Zhang, M. *et al.* Calmodulin (CaM) Activates PI3Kα by Targeting the "Soft" CaM-Binding Motifs in Both the nSH2 and cSH2 Domains of p85α. *J Phys Chem B* **122**, 11137-11146 (2018).
56 Nguyen, D. *et al.* Identification and Characterization of a B-Raf Kinase α-Helix Critical for the Activity of MEK Kinase in MAPK Signaling. *Biochemistry* **59**, 4755-4765, doi:10.1021/acs.biochem.0c00598 (2020).
57 Cope, N. *et al.* Biochemical Characterization of Full-Length Oncogenic BRAF(V600E) together with Molecular Dynamics Simulations Provide Insight into the Activation and Inhibition Mechanisms of RAF Kinases. *Chembiochem* **20**, 2850-2861, doi:10.1002/cbic.201900266 (2019).
58 Kim, J. *et al.* A dynamic hydrophobic core orchestrates allostery in protein kinases. *Sci Adv* **3**, e1600663 (2017).
59 Modi, V. & Dunbrack, R. L. Defining a new nomenclature for the structures of active and inactive kinases. *Proceedings of the National Academy of Sciences of the United States of America* **116**, 6818-6827, doi:10.1073/pnas.1814279116 (2019).

60 McSkimming, D. I., Rasheed, K. & Kannan, N. Classifying kinase conformations using a machine learning approach. *BMC Bioinformatics* **18**, 86 (2017).
61 Weber, C. K., Slupsky, J. R., Kalmes, H. A. & Rapp, U. R. Active Ras induces heterodimerization of cRaf and BRaf. *Cancer Res* **61**, 3595-3598 (2001).
62 Patton, E. E. *et al.* in *Curr Biol* Vol. 15 249-254 (2005).
63 Lavoie, H. & Therrien, M. in *Nat Rev Mol Cell Biol* Vol. 16 281-298 (2015).
64 Thevakumaran, N. *et al*. in *Nat Struct Mol Biol* Vol. 22 37-43 (2015).
65 Shaw, A. S., Kornev, A. P., Hu, J., Ahuja, L. G. & Taylor, S. S. Kinases and pseudokinases: lessons from RAF. *Mol Cell Biol* **34**, 1538-1546 (2014).
66 Zhang, M., Jang, H. & Nussinov, R. PI3K Driver Mutations: A Biophysical Membrane-Centric Perspective. *Cancer Research* **81**, 237-247, doi:10.1158/0008-5472.Can-20-0911 (2021).

Table 1 Initial Configurations of the simulated systems of monomeric B-Raf. The distance between Lys483 and Glu501 is measured between the β-carbon atoms and is calculated after modeling missing residues and performing energy minimization steps. R_g is the radius of gyration.

	configuration	PDB	K483 - E501 Distance (Å)	αC -helix	A-loop	AS-H1	A-loop R_g (Å)
V600E:	a	4MNE	7.81	in	extended	no	0.86
	b	4MNE	9.07	in	extended	no	0.88
	c	6U2H	7.81	in	extended	no	0.82
	d	3OG7	8.32	in	extended	no	0.76
	e	4MNF	7.89	in	extended	no	0.87
	f	5ITA	10.16	intermediate	extended	no	0.85
	g	5ITA	10.75	intermediate	collapsed	yes	0.62
	h	4XV2	12.26	out	collapsed	no	0.68
	i	6U2G	13.03	out	collapsed	yes	0.64
wild-type:	j	4MNE	8.03	in	extended	no	0.86
	k	6U2H	7.37	in	extended	no	0.79
	l	5ITA	11.12	intermediate	collapsed	yes	0.67
	m	6U2G	14.16	out	collapsed	yes	0.60

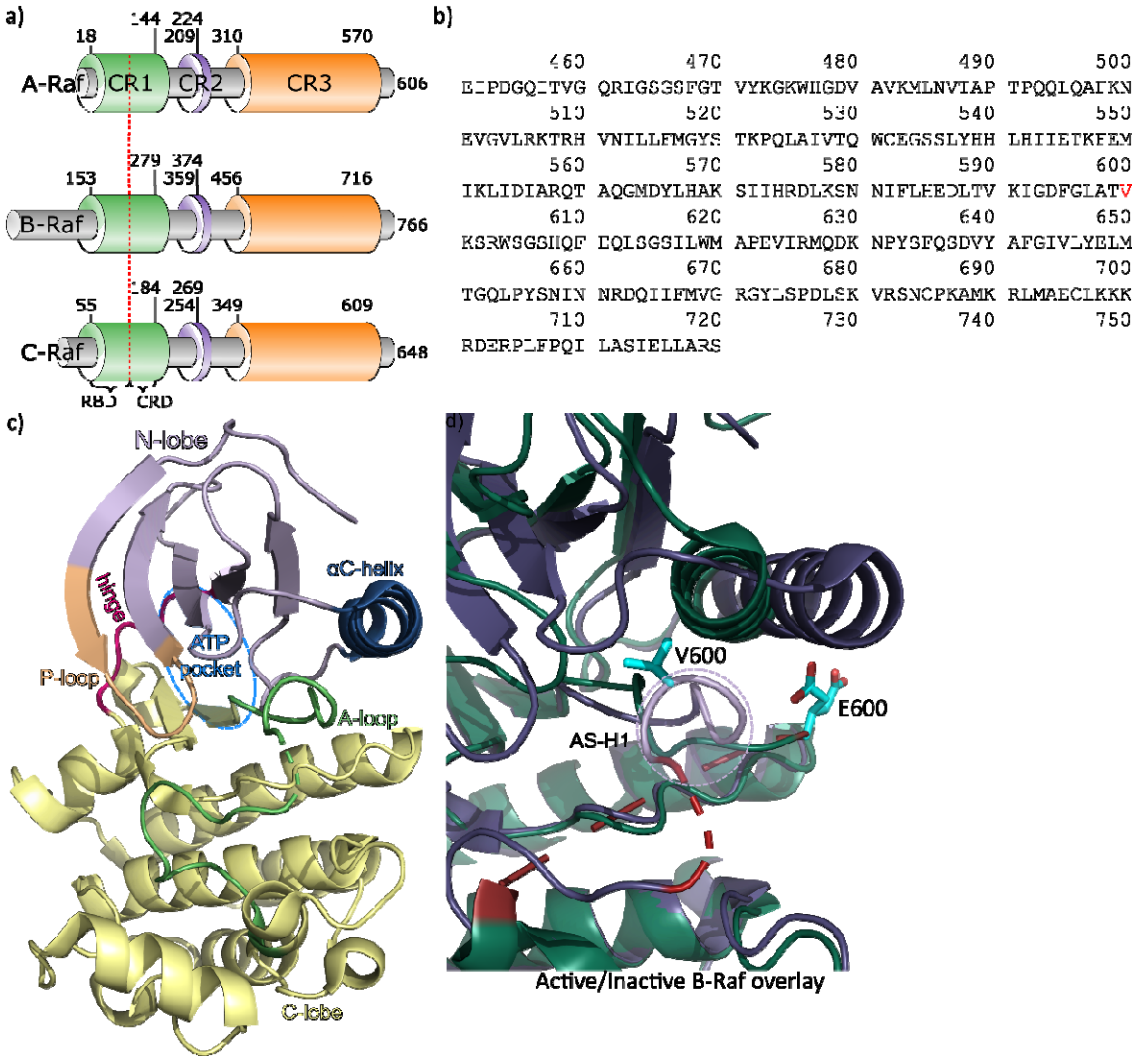

Figure 1 B-Raf structure and key features of the kinase domain. a) Conserved regions of Raf family proteins b) B-Raf kinase domain sequence. Residue Val600 is denoted in red. c) B-Raf kinase domain crystal structures for inactive wild-type B-Raf. Close up of A-loop and αC-helix for B-Raf V600E (4MNF, teal) and inactive wild-type B-Raf (6U2G, purple). Missing residues are denoted by dashed red lines.

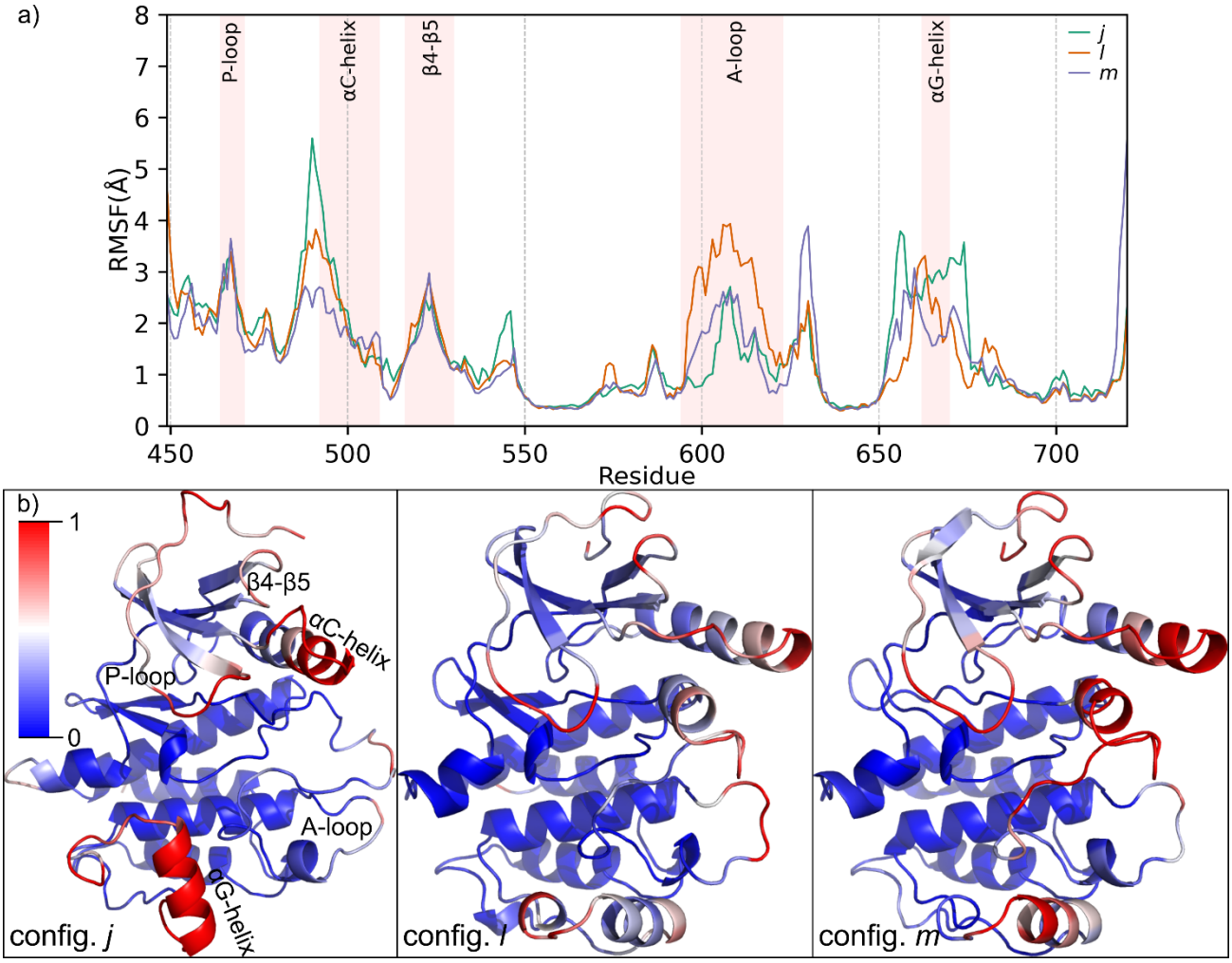

Figure 2 B-Raf exhibits peaks in residue fluctuation in the P-loop, residues before the αC-helix, A-loop, and around the αG-helix. a) RMSF for residues in wild-type B-Raf configurations *j* (green), *l* (orange), and *m* (purple). b) Snapshot of configuration *j*, *l*, and *m* colored by normalized b-factor value from maximum b-factor (red) to minimum b-factor (blue).

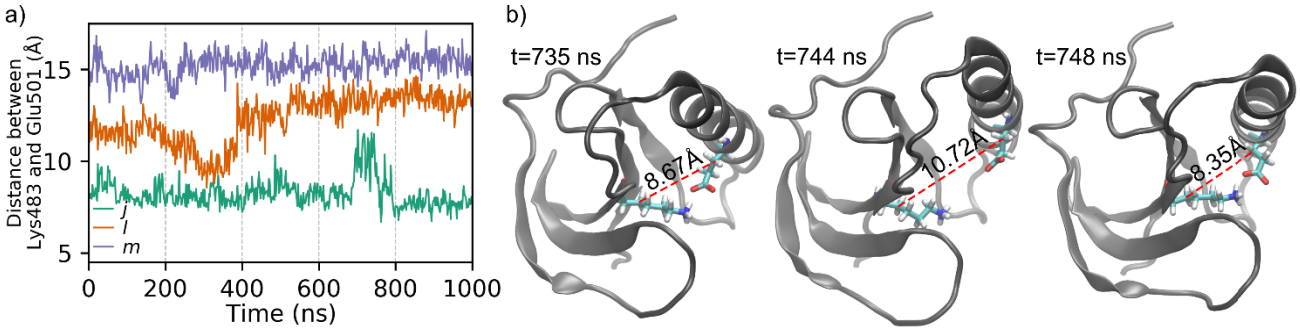

Figure 3 Wild-type B-Raf αC-helix position. a) Distance between Lys483 and Glu501 over the course of the simulations for wild-type B-Raf configurations *j* (green), *l* (orange), and *m* (purple). b) Snapshots representing the salt bridge interaction between Lys483 and Glu501 at selected times of *t* = 735, 744, and 748 ns for configuration *j*.

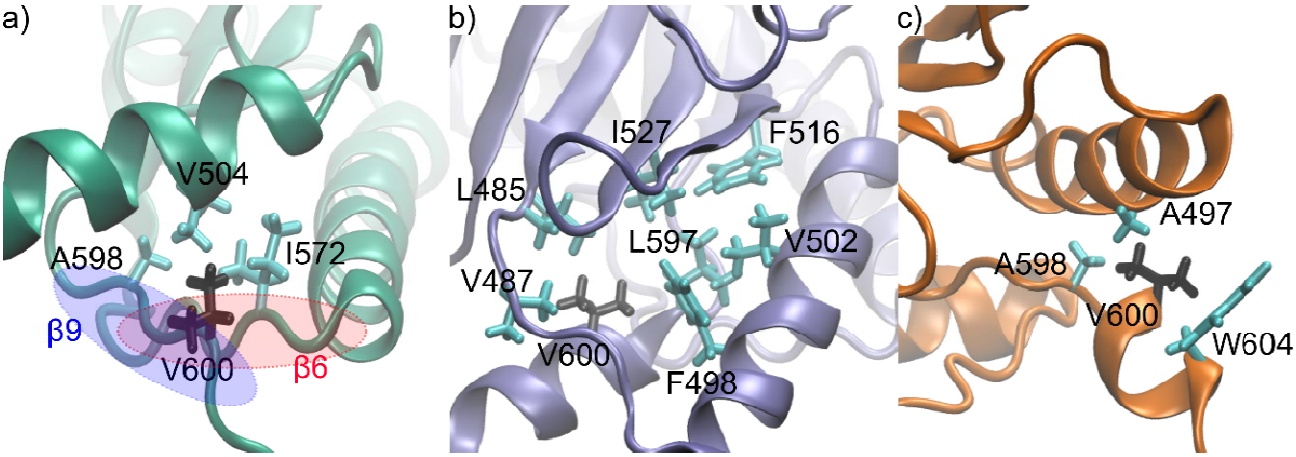

Figure 4 Hydrophobic interactions between V600 and neighboring residues stabilize the extended or collapsed A-loop. a) Hydrophobic residues (cyan) around Val600 (black) and hydrogen bonding between β6 (red) and β9 (blue) stabilize the extended A-loop in configuration *j*. b) Hydrophobic residues (cyan) form a pocket that contains Val600 (black) and stabilizes the collapsed A-loop configuration in configuration *m*. c) The extended A-loop with inhibitory helix of configuration *l* helix lacks the large hydrophobic pocket of configuration *m*, and the hydrogen bonding β-sheet interactions of configuration *j*.

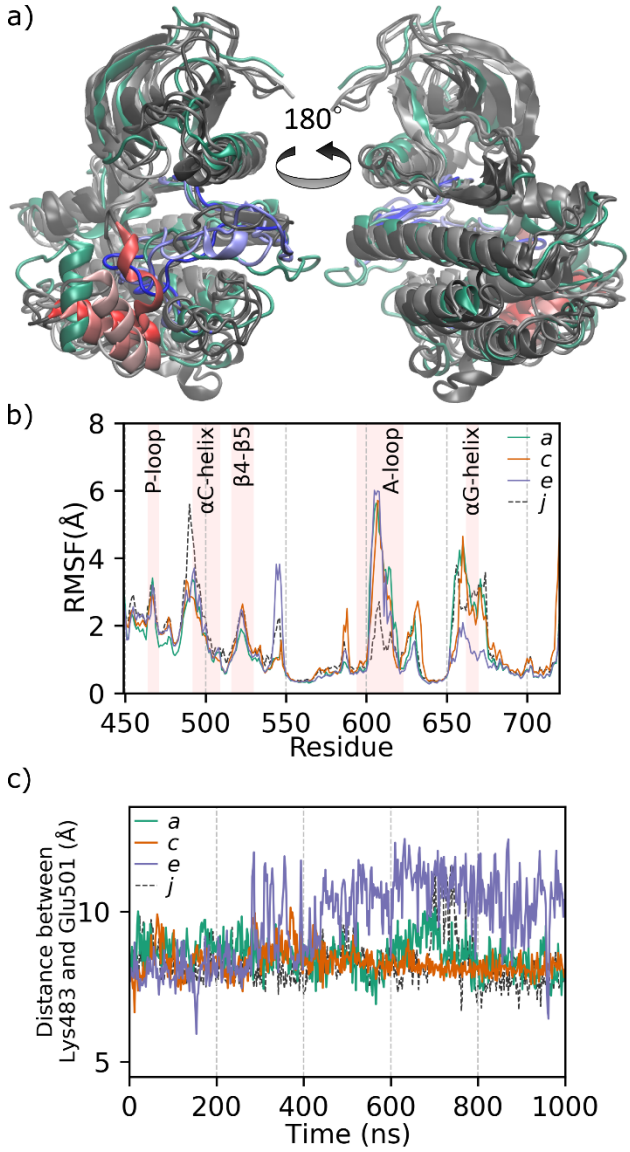

Figure 5 Active B-Raf V600E exhibits many of the same features as active wild-type B-Raf. a) Snapshots of active wild-type B-Raf (configuration *j*, green) and B-Raf V600E (configurations *a*-*d*, light gray-dark gray). The αG-helix of the B-Raf V600E structures are depicted in red and the activation loop is depicted in blue. b) RMSF for kinase domain residues for B-Raf V600E configurations *a* (green), *c* (orange), and *e* (purple) that began with an inward αC-helix. c) Distance between Lys483 and Glu501 over the course of the simulations for B-Raf V600E configurations that began with an inward αC-helix *a* (green), *c* (orange), and *e* (purple). A comparable wild-type B-Raf, configuration *j*, is shown in the black dashed line in each figure.

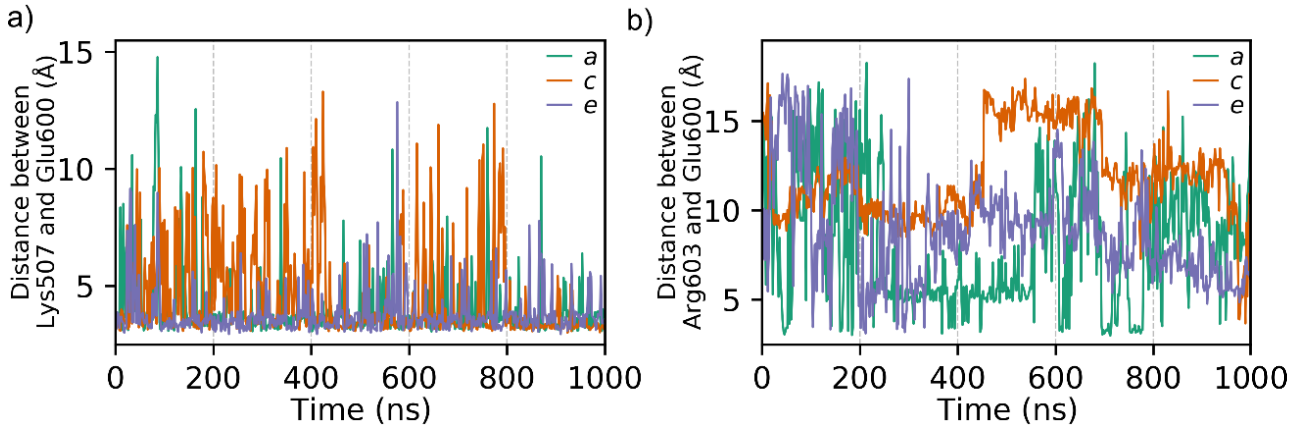

Figure 6 The salt bridge between Glu600 and Lys507 stabilizes the extended A-loop in active B-Raf V600E. Distance between Glu600 and a) Lys507 and b) Arg603 for configurations that began with an inward αC-helix: a (green), c (orange), and e (purple).

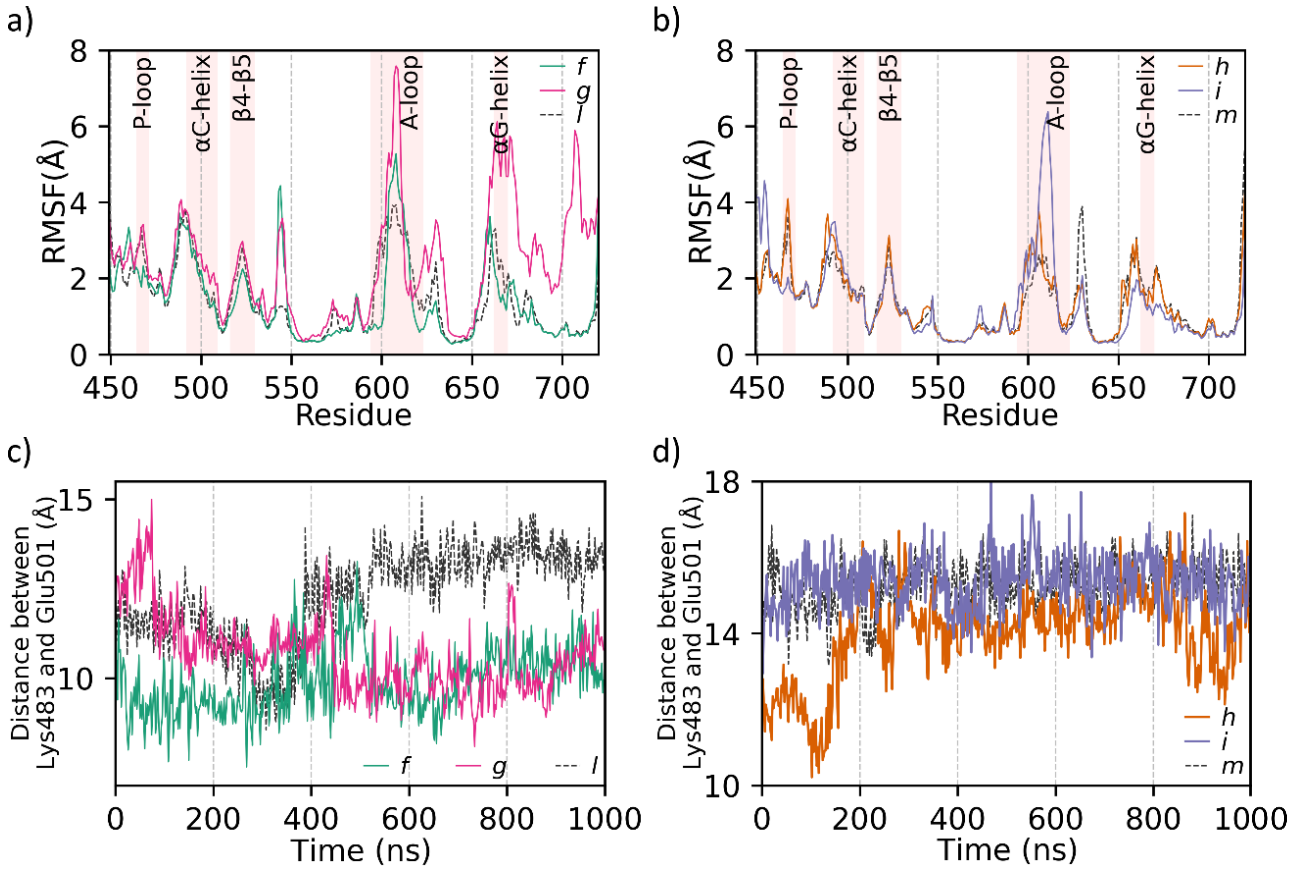

Figure 7 B-Raf V600E with intermediate and outward αC-helix do not change to an inward αC-helix. RMSF for kinase domain residues for B-Raf V600E configurations that began with an a) intermediate αC-helix, *f* (green) and *g* (pink) or b) outward αC-helix, *h* (orange) and *g* (purple). Distance between Lys483 and Glu501 through the course of the simulation for B-Raf V600E configurations that began with an c) intermediate αC-helix or d) outward αC-helix. A comparable wild-type B-Raf system is shown in the black dashed line in each figure.

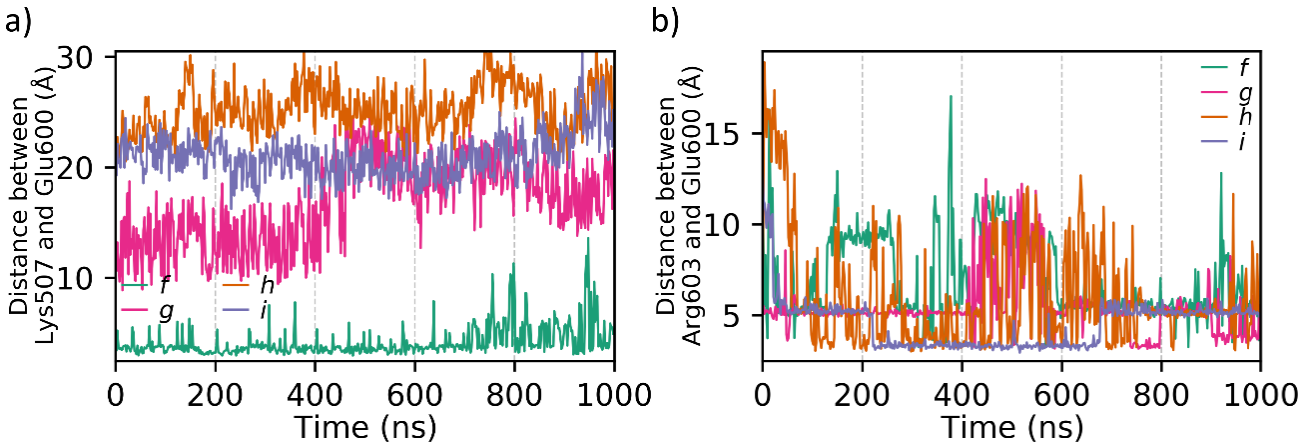

Figure 8 The salt bridge between Glu600 and Arg603 stabilizes the collapsed A-loop in inactive B-Raf V600E. Distance between Glu600 and a) Lys507 and b) Arg603 for B-Raf V600E configurations that began with an intermediate or outward αC-helix: *f* (green), *g* (pink), *h* (orange), and *e* (purple).

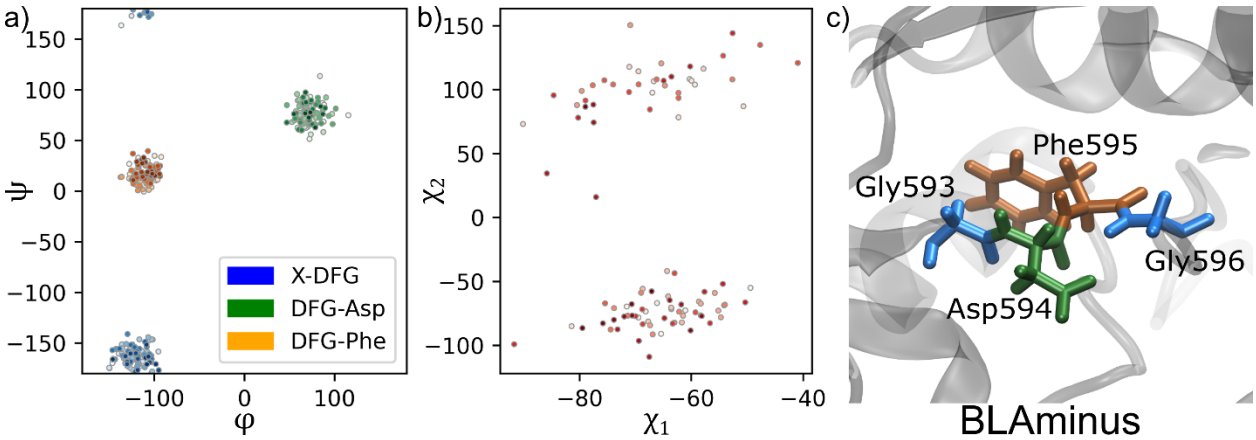

Figure 9 Active B-Raf adopts a BLAminus XDFG orientation. a) Ramachandran graph, b) side chain dihedral angles, and c) representative snapshot of the residues ^{593}GDFG^{596} for configuration *j*. Lightly colored symbols represent data from early in the simulation, darkly colored symbols are from the end of the simulation.

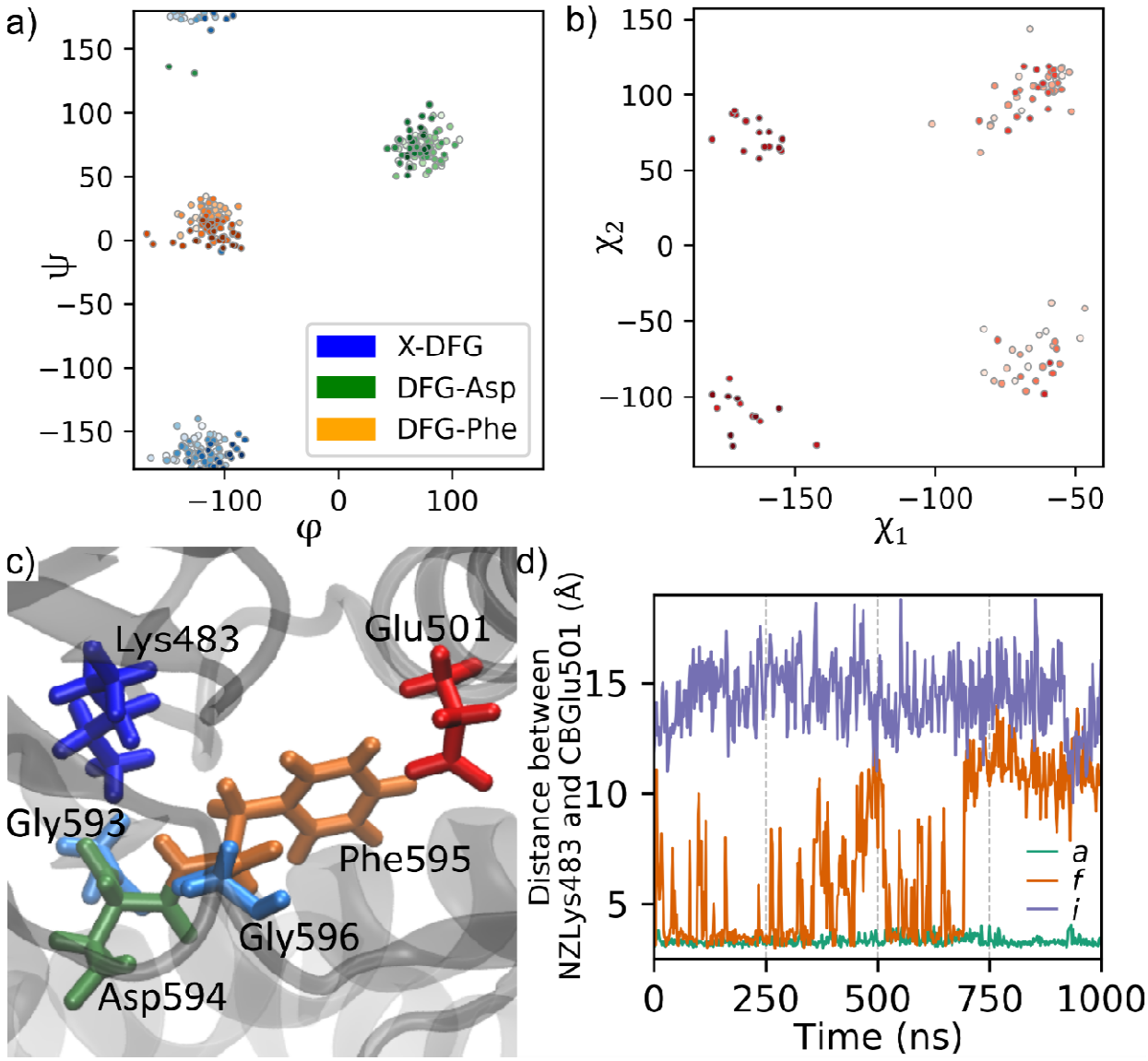

Figure 10 Phe595 trans χ_1 rotamer disrupts the salt bridge between Lys483 and Glu501, resulting in an outward αC-helix a) Ramachandran graph, b) side chain dihedral angles, and c) representative snapshots of the residues ^{593}GDFG^{596} for configuration *f*. Lightly colored symbols represent data from early in the simulation, darkly colored symbols are from the end of the simulation. d) Distance between the amide nitrogen of Lys483 and the carboxylate carbon of Glu501 for configuration *f* (orange). A representative system in which the αC-helix is always in (configuration *a*, green) and always out (configuration *i*, purple) are provided for comparison.

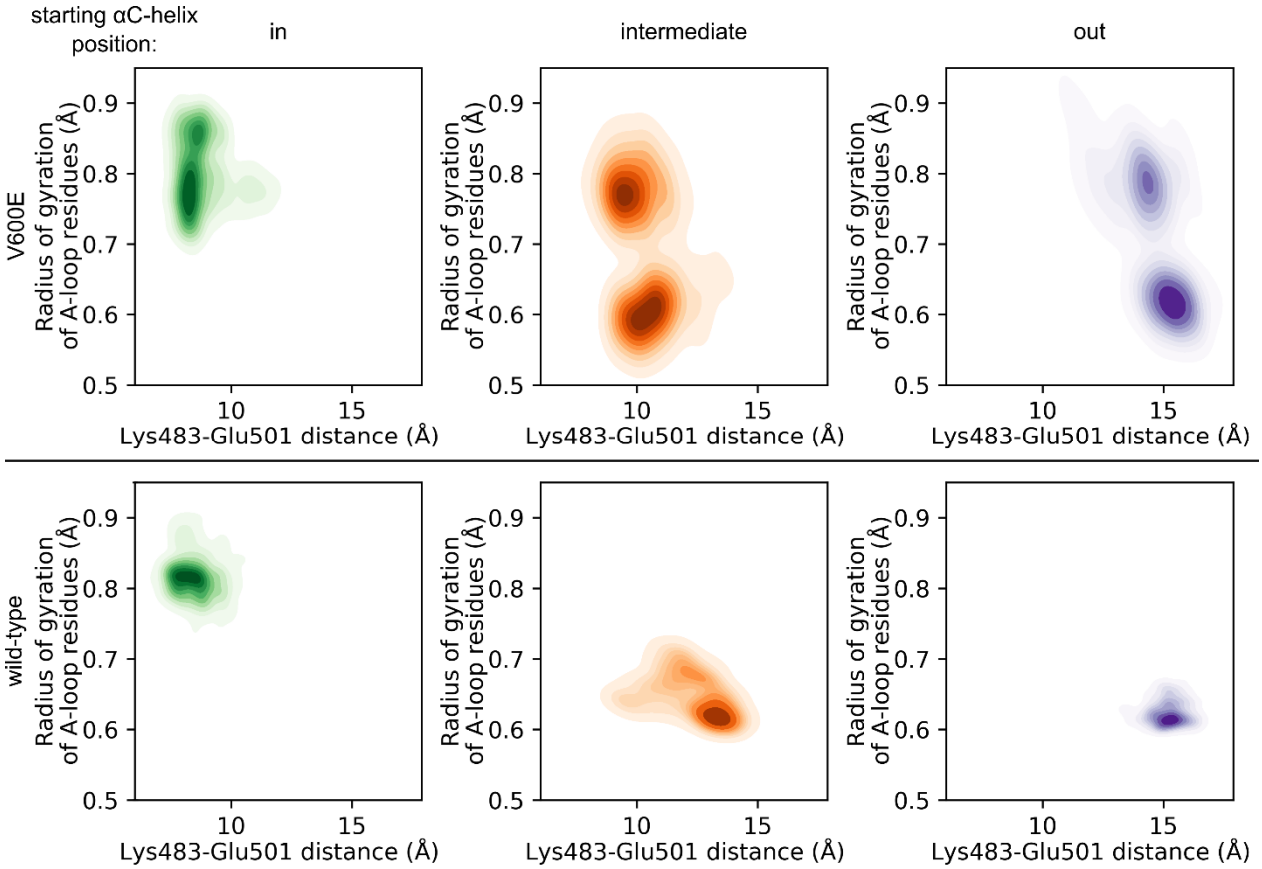

Figure 11 Probability distribution of radius of gyration of activation loop residues versus the distance between Lys483 and Glu501 shows that the B-Raf V600E results in a more flexible A-loop. Simulations that began with an inward orientated αC-helix are in green, intermediate αC-helix in orange, and outward αC-helix in purple. Results from B-Raf V600E simulations are shown in the top row and wild-type simulations are in the bottom row.